Check for updates

Increasing ocean stratification over the past half-century

Guancheng Li [1,2,3], Lijing Cheng [1,2,3 ✉], Jiang Zhu [1,2,3 ✉], Kevin E. Trenberth [4], Michael E. Mann [5] and John P. Abraham[6]

Seawater generally forms stratified layers with lighter waters near the surface and denser waters at greater depth. This stable configuration acts as a barrier to water mixing that impacts the efficiency of vertical exchanges of heat, carbon, oxygen and other constituents. Previous quantification of stratification change has been limited to simple differencing of surface and 200-m depth changes and has neglected the spatial complexity of ocean density change. Here, we quantify changes in ocean stratification down to depths of 2,000 m using the squared buoyancy frequency N^2 and newly available ocean temperature/salinity observations. We find that stratification globally has increased by a substantial 5.3% [5.0%, 5.8%] in recent decades (1960–2018) (the confidence interval is 5–95%); a rate of 0.90% per decade. Most of the increase (~71%) occurred in the upper 200 m of the ocean and resulted largely (>90%) from temperature changes, although salinity changes play an important role locally.

Most solar heating is absorbed at Earth's surface, primarily the ocean surface. This creates warm moist air near the surface and low-level atmospheric instability that is stabilized by convection. Below the ocean surface, however, it leads to warmer waters atop cooler ones and a stable overall configuration (Fig. 1a and Extended Data Fig. 1a). Salinity, associated with the difference between evaporation E and precipitation P $(E–P)$ (Extended Data Fig. 1b), partially regulates this configuration. This inverse relationship between the stability of the ocean and atmosphere has important climatological implications.

Ocean stratification is quantified by density change with depth, which in turn, is determined by the vertical distribution of temperature and salinity, in addition to pressure. The zonal mean climatological density distribution (Fig. 1a) shows lighter seawater above the denser water, with bowed isopycnals in the upper 700 m, mainly reflecting ocean heating and impact of the ocean general circulation (for example, subtropical overturning). Stable stratification inhibits vertical mixing and impacts the vertical exchanges of heat, carbon, dissolved oxygen and nutrients[1–7].

As human-caused greenhouse warming has fundamentally altered oceanic temperature and salinity fields, impacts to stratification are expected[8,9]. An increase in near-surface stratification during the second half of the twentieth century has been documented[1,10,11] but characterization of the temporal and spatial changes in stratification have been controversial. In the Intergovernmental Panel on Climate Change Fifth Assessment Report (IPCC-AR5)[1], ocean thermal stratification between 0 and 200 m depth was approximately represented by the global mean temperature difference between the 0-m and 200-m layers. That analysis suggested a stratification increase of ~4% from 1971 to 2010 (~1% per decade) and no error estimate was given. The more recent IPCC Specific Report on the Ocean and Cryosphere in a Changing Climate (SROCC)[10] estimated a 2.18–2.42% stratification increase from 1971–1990 to

1998–2017 (~0.85 ± 0.04% per decade), using the globally averaged square of the buoyancy frequency (N^2) based on the density difference between the layers 0–10 m and 190–210 m. The SROCC estimate is smaller than the IPCC-AR5 estimate by ~15%, despite being based on a more recent period, when global warming-induced changes should be even greater. These disparities and the different methods emphasize the uncertainty in our knowledge of past stratification changes.

This uncertainty results from incomplete observational data (discussed further below) and which ocean layers are used. Ocean temperature and salinity observations are somewhat sparse and unevenly distributed in space[12]. They are also subject to instrumental biases[8,12]. Moreover, using the density difference between two single layers: 0 versus 200 m in AR5 (0–10 m versus 190–210 m in SROCC) is a crude approximation of the ocean stratification. Those two layers do not reflect the full vertical structure of ocean changes and stratification, and uncertainties therein[13]. Besides, both the pycnocline and thermocline in many regions are either shallower or deeper than 200 m (Fig. 1b and Extended Data Fig. 1b).

The present study adopts the recently improved temperature and salinity estimates (denoted as Institute of Atmospheric Physics, IAP data[14,15]; Methods) to better quantify long-term changes in stratification in the upper 2,000 m of the world oceans over the past half-century. We also create the continuous N^2 field from the sea surface to 2,000 m of depth, computed from the vertical density gradient rather than from the density difference between only the surface and 200-m layers (Fig. 1; Methods), which allows a full quantification of the spatial structure of changes in stratification.

Quantification of stratification

The mean N^2 within 1981–2010 defines the mean vertical stratification in the ocean, that is $N^2 > 0$, as density increases with depth (Fig. 1a versus 1c). The zonal mean value of N^2 is largest within

[1]International Center for Climate and Environment Sciences, Institute of Atmospheric Physics, Chinese Academy of Sciences, Beijing, China. [2]Center for Ocean Mega-Science, Chinese Academy of Sciences, Qingdao, China. [3]University of Chinese Academy of Sciences, Beijing, China. [4]National Center for Atmospheric Research, Boulder, CO, USA. [5]Department of Meteorology and Atmospheric Science, Department of Geosciences, and Earth and Environmental Systems Institute, Pennsylvania State University, State College, PA, USA. [6]School of Engineering, University of St. Thomas, St Paul, MN, USA. ✉e-mail: chenglij@mail.iap.ac.cn; jzhu@mail.iap.ac.cn
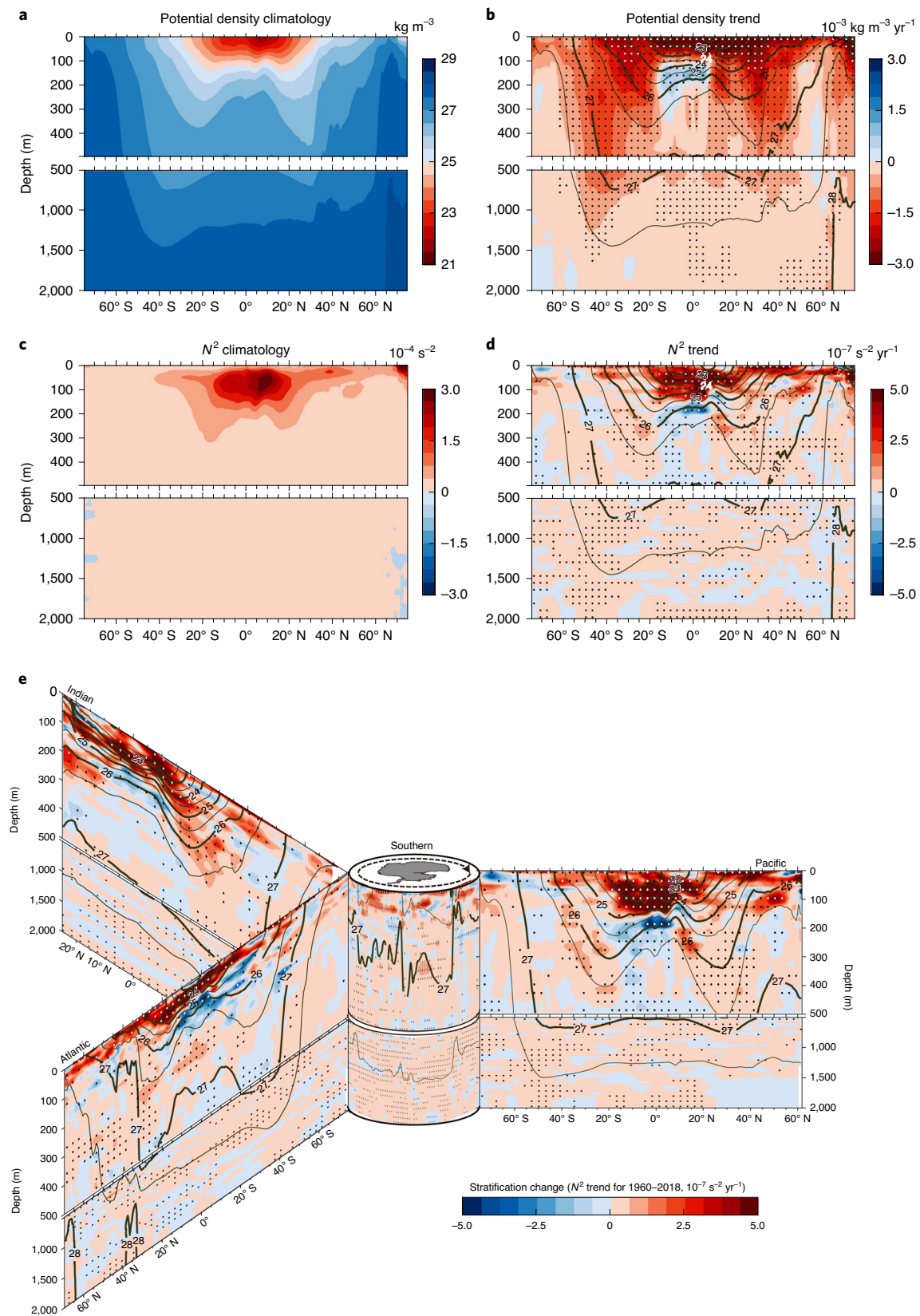
Fig. 1 | Climatological mean and long-term trends for global mean ocean density and squared buoyancy frequency (N^2) over 1960–2018.
a,c, Climatological and zonal mean potential density (**a**) and N^2 (**c**) for 1981–2010. **b,d**, Long-term linear trends for 1960–2018 in potential density (**b**) and N^2 (**d**). The stippled areas in **b** and **d** denote the signals significant at 90% confidence level, accounting for the spatial sampling and instrumental uncertainty. **e**, Zonal and vertical sections of the 0–2,000 m N^2 trends during 1960–2018 in the three main basins (Pacific, Atlantic and Indian) surrounding the meridional mean section of the Southern Ocean (30° S). Black contour lines show the climatology of potential density with 0.5 kg m^{-3} intervals.
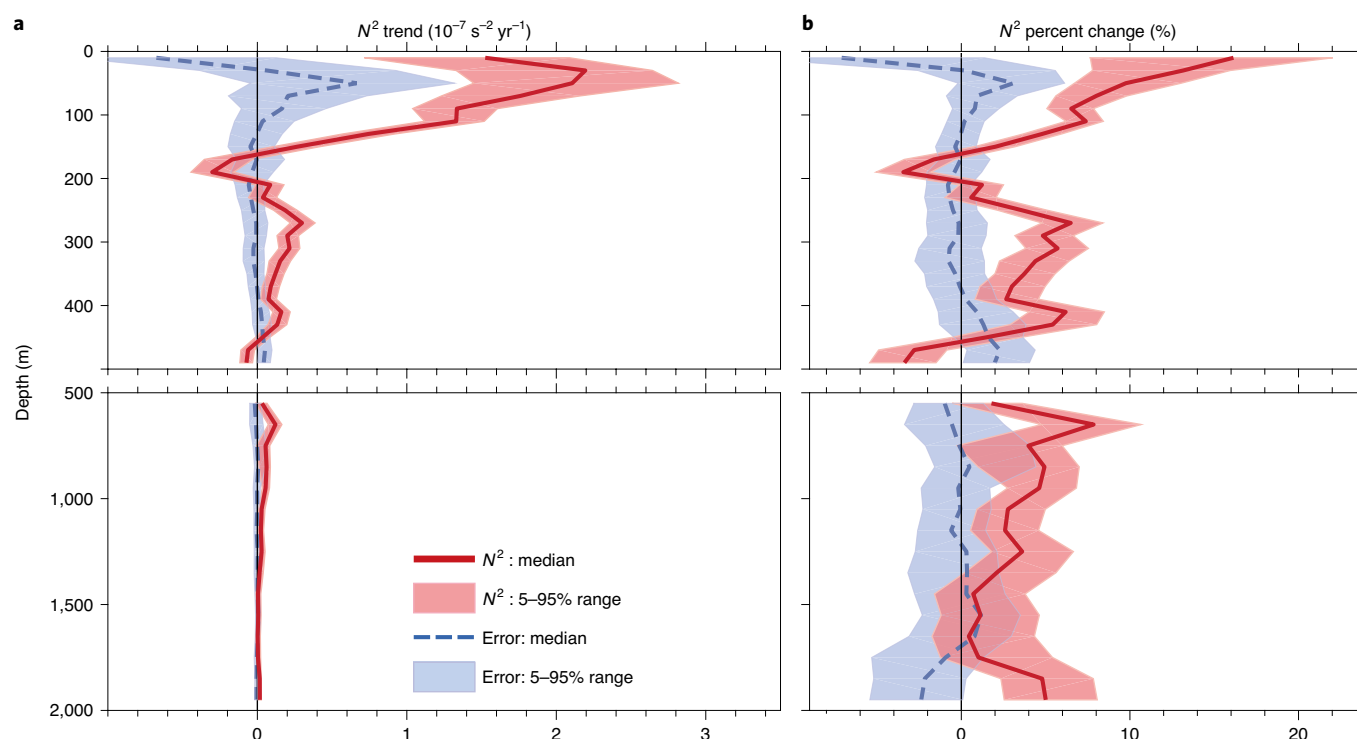
Fig. 2 | Trends of N^2 over depth and the percent change. a, Linear trend of global mean N^2 from surface to 2,000 m, with an interval of 20 m for the upper 500 m and 100 m below 500 m. **b**, Same as for **a** but for percentages of long-term changes of global mean N^2 relative to their 1981–2010 average. The solid line is the N^2 estimate by this study and the dotted line is the total error, including sampling and instrumental errors. The shadings denote their 90% CIs.

50–300 m depths in low latitudes (20° S–20° N) and corresponds to the greatest density gradient in the thermocline layer (Extended Data Fig. 1a). Larger N^2 is also apparent in the upper 200 m of the northern polar regions (north of 60° N), associated with more freshwater in the upper Arctic Ocean (Extended Data Fig. 1c).

Since 1960, ocean density has experienced a substantial decrease in almost all zonal bands from the surface to depths of 2,000 m (Fig. 1b) that is much sharper in the upper layers than in the deep ocean and corresponds to a broad increase in N^2 (Fig. 1d,e), especially near the thermocline (within 23–25 kg m^{-3} isopycnals). A notable exception is the 100–300-m layer in the tropics (10° N–20° S), where the density increase (Fig. 1b) is due to the cooling in the Indian and Pacific Oceans and weaker warming in the Atlantic section in these layers[1] (Extended Data Fig. 1b). These signals are associated with the southward shift of equatorial cooling waters, which may be driven by the meridional displacement and intensification of subtropical gyres in all three ocean basins[1,10] (Fig. 1e). Trends in N^2 are larger and tend to be significant where there are strong vertical differences in the density trend (Fig. 1b versus 1d), because N^2 depends on the vertical density gradient.

This N^2 structure is broadly consistent across all three major basins (Fig. 1e) but decreases extend deeper in the tropical Pacific Ocean (150–200 m) than the tropical Atlantic and Indian Oceans (100–150 m), consistent with its deeper thermocline. The stratification increase in the North Atlantic for the upper 100 m is reported to be responsible for the weakening of deep ocean overturning circulation[1,16] (Fig. 1e). In the tropics, it shows a strong N^2 increase for the upper 300 m, while in the middle and high latitudes, the significant N^2 increase appears mostly below 500 m (Fig. 1d,e), because the signals from the near-surface ocean subduct into subsurface ocean due to deeper mixed layer (Extended Data Fig. 1) and then change the stratification (Fig. 1). This indicates the importance of ocean dynamics (mixed layer and subduction process) in the change of N^2.

In the global average, the N^2 (Fig. 2a) changes are more pronounced in the upper 200 m than below, consistent with stronger temperature and salinity changes there (Extended Data Fig. 1b,d). The maximum N^2 increase occurs within 20–100 m. However, as the climatological mean stratification in the deep ocean is small (weaker vertical density gradient in the deep layer, Fig. 1a,c), small absolute changes can still reflect potentially important relative changes (Fig. 2b), the latter of which are defined as the linear trends in N^2 during the 1960–2018 interval divided by the climatological mean to give the fractional change (Fig. 2b). The bias-corrected IAP estimates show a 5–18% increase in stratification in the upper 150 m and a 0–8% increase for 220–2,000 m, indicating a clear stratification increase in the upper 2,000 m ocean waters (except layers around 200 m, discussed above). The total N^2 increase within 0–200 m contributes to ~71% of the overall 0–2,000 m increase. Below 500 m, both the trends and percentages are less robust than in the upper layer, owing to both fewer observations and weak trends.

Global and basin N^2 time series

The global (0–2,000 m) average N^2 time series (Fig. 3a) shows a robust upward trend since the early 1960s that reflects the increase of global ocean stratification. The IAP estimate yields a total 0–2,000 m N^2 change of 1.5 [1.4, 1.7] × 10^{-8} s^{-2} yr^{-1} over the period 1960–2018 (see Table 1). The corresponding rate is 10.7 [9.9, 11.4] × 10^{-8} s^{-2} yr^{-1} for 0–200 m. This is equal to 5.3 [5.0, 5.8]% overall and 6.9 [6.3, 7.3]% for the 0–200 m stratification increase, based on a climatological mean state from 1981 to 2010. All four major basins have experienced robust increases of stratification since 1960, with the strongest rate in the southern oceans (south of 30° S, 7.9 [6.8, 9.6]%), followed by the Pacific Ocean (Supplementary Table 1, 5.6 [5.2, 5.9]%), the Atlantic Ocean (4.1 [3.5, 4.6]%) and then the Indian Ocean (3.7 [3.4, 4.2]%). Hence, the long-term increasing trends of N^2 and their zonal patterns (Figs. 1 and 3)

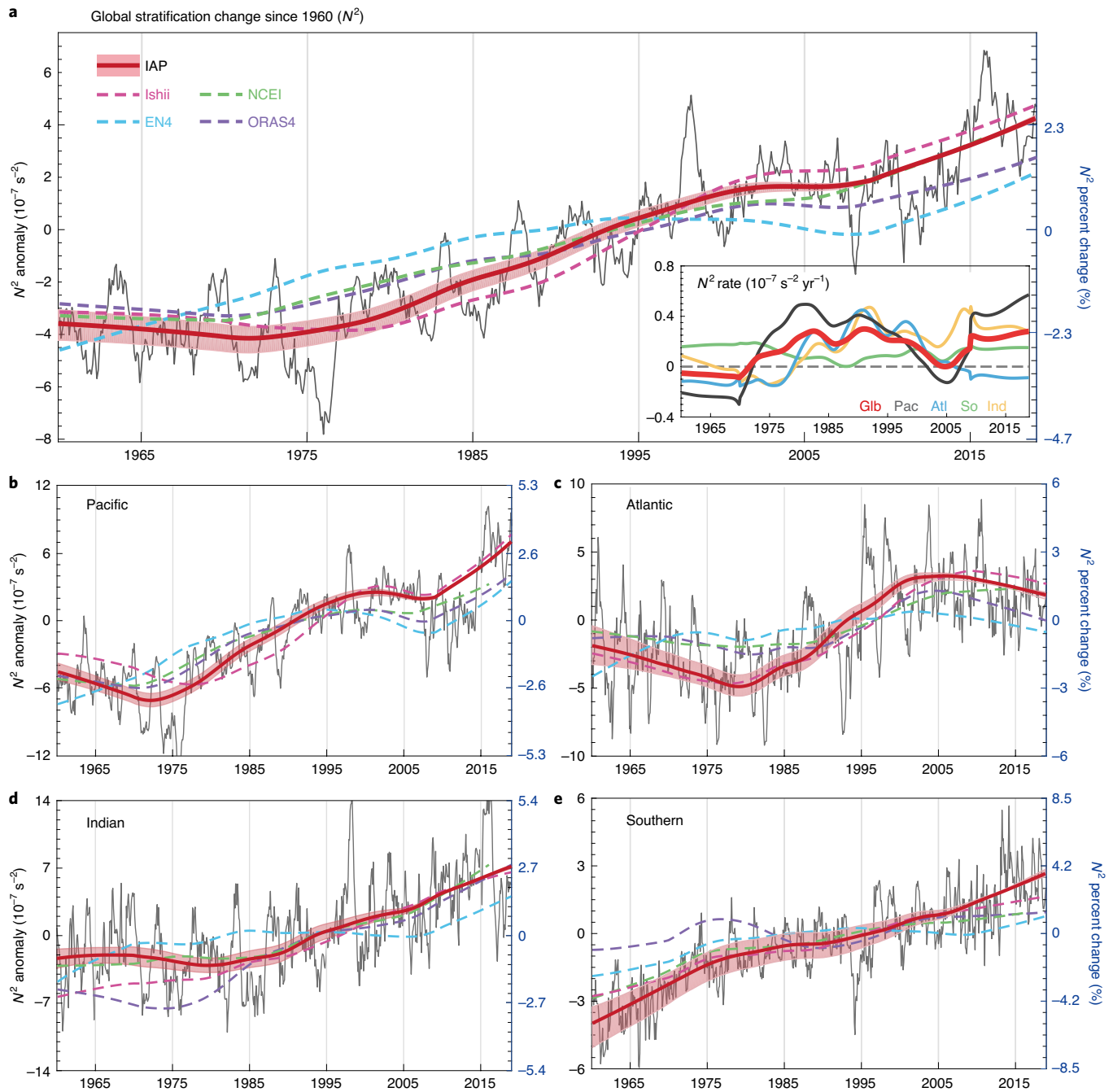**Fig. 3 | Time evolution of the 0–2,000 m ocean stratification changes. a–e,** Global (**a**), Pacific (**b**), Atlantic (**c**), Indian (**d**) and Southern (**e**) Oceans. The thick lines are after application of a LOWESS (locally weighted scatterplot smoothing) smoother (span width of 20 yr) to depict the interdecadal and longer-term changes. The 90% CI for IAP estimates (shading) account for both spatial sampling of historical observations and instrumental errors. The IAP monthly anomaly time series indicate how aliasing of interannual variations occurs in N^2 (thin grey lines). All time series are relative to a 1981–2010 baseline. The inset in panel **a** shows the global and basin mean rates of N^2 calculated by centred differences of the smoothed time series: Glb, Global; Pac, Pacific; Atl, Atlantic; So, Southern; Ind, Indian.

reveal a robust human-driven change in the ocean in addition to the long-term temperature and salinity change structures (Extended Data Fig. 1) previously attributed to human activities[17–19].

These results show a stronger trend than other products 3.0 ± 1.0% (EN4; ref. [20]), 4.5 ± 1.0% (NCEI; ref. [21]) and 3.7 ± 1.2% (ORAS4; ref. [22]), with the exception of Ishii[23] (5.7 ± 1.3%) (Table 1). The present results also show stronger global stratification changes than reported in the IPCC-AR5 (using NCEI) and SROCC (using EN4)[1,10]. Because our results are for different layers (0–2,000 m and

0–200 m) and 1960–2018, which differ from those reports, and the calculation methods are also different, we now adopt the same methods as IPCC (summarized in Table 1). The IAP data show a 5.1 ± 2.1% increase in upper 200 m stratification during 1971–2010, 28% stronger than AR5 (~4%). Further, IAP shows a 4.3% increase from 1971–1990 to 1998–2017 (Table 1), which is ~87% stronger than SROCC (~2.3%).

The data biases in traditional datasets are mainly responsible for their underestimations (see Supplementary Information for

Table 1 | Climatology ($10^{-8}\,s^{-2}$), trend ($10^{-8}\,s^{-2}\,yr^{-1}$) and percent change (%) of the global mean of squared buoyancy frequency (N^2) during 1960–2018

Global mean		0–200 m	0–500 m	0–1,000 m	0–2,000 m
Climatology		9,387 ± 468	5,089 ± 125	2,993 ± 38	1,687 ± 39
IAP	Trend	10.7 [9.9–11.4]	5.0 [4.6–5.4]	2.9 [2.6–3.1]	1.5 [1.4–1.7]
	Percent	6.9 [6.3–7.3]	5.9 [5.4–6.4]	5.7 [5.2–6.2]	5.3 [5.0–5.8]
Ishii	Trend	11.5 ± 3.8	5.6 ± 1.4	3.0 ± 0.7	1.6 ± 0.4
	Percent	7.1 ± 2.4	6.4 ± 1.6	5.8 ± 1.3	5.7 ± 1.3
EN4	Trend	6.9 ± 4.4	2.7 ± 1.2	1.5 ± 0.6	0.9 ± 0.3
	Percent	4.2 ± 2.7	3.1 ± 1.4	3.0 ± 1.1	3.0 ± 1.0
ORAS4	Trend	7.9 ± 4.6	3.4 ± 1.3	1.9 ± 0.7	1.1 ± 0.3
	Percent	5.1 ± 3.0	4.0 ± 1.5	3.8 ± 1.3	3.7 ± 1.2
NCEI	Trend	10.4 ± 3.0	4.4 ± 1.0	2.4 ± 0.5	1.3 ± 0.3
	Percent	6.7 ± 2.0	5.2 ± 1.2	4.8 ± 1.0	4.5 ± 1.0
Percent (%)	IPCC	IAP	Ishii	EN4	ORAS4
AR5 (T_{0-200}) (1971–2010)	4	5.1 ± 2.1	4.2 ± 1.7	1.0 ± 3.0	3.7 ± 1.8
SROCC (N^2) (1998–2017 versus 1971–1990)	2.18–2.42	4.3	4.1	0.5	2.6

Uncertainty range indicates 90% CI. Lower panel shows the percent change (%) of the global stratification when adopting the IPCC-AR5 and SROCC methods and time periods.

discussions and tests, Extended Data Figs. 2 and 3 and Supplementary Figs. 1 and 2). The major error comes from sparse sampling of observations in the top 2,000 m ocean waters and instrumental errors. A well-identified 'conservative bias' in these traditional data products (EN4, NCEI and ORAS4), arises from an initial assumption of climatological values in poorly observed regions which leads to underestimation of ocean warming trends from the surface to 2,000 m (refs. [9,14,24]). Insufficient vertical sampling in observations poses an additional error associated with vertical interpolation methods (Extended Data Fig. 4). This issue has not been quantified in available products but is an important source for interproduct differences (Supplementary Information, notably Supplementary Table 2). Here, this uncertainty is quantified using high-resolution observations through a vertical subsample test. Because it reveals an overall uncertainty in long-term N^2 trends of <5% for IAP methodologies (Methods; Extended Data Figs. 5–7), the IAP results are less biased than other results presented and the uncertainty associated with these error sources is well quantified (Methods). Further, the accuracy for IAP estimate is improved by using the bias correction associated with these error sources. All these considerations motivate the use of IAP data, which provides the best unbiased estimate of N^2 changes and its uncertainty.

The interannual stratification fluctuations are dominated by the El Niño/Southern Oscillation (ENSO), with a significant correlation of ~0.55 between the global mean N^2 (~0.64 for Pacific mean) with an ENSO index (Niño 3.4 index[25]) (Fig. 3 and Extended Data Fig. 8). This is probably due to the strong thermocline variations and formation of barrier layers associated with ENSO[26,27].

Past work has demonstrated that the long-term trends in ocean temperature, salinity and heat content impacting global mean N^2 are driven primarily by anthropogenic forcing[15,28]. There is, nonetheless, superimposed on these trends substantial decadal variability with two rapid increases from 1978 to 1996 and 2014 to present (Fig. 3a). The reduced trend in global N^2 during 1997–2013 is consistent with the slowdown in surface warming over that timeframe, which has been demonstrated to result from both forced and internal variability[29–33]. The latter is dominated by Pacific decadal sea surface temperature (SST) changes (Fig. 3a versus 3b), as noted in previous work[32,34].

Temperature and salinity contributions

Temperature changes raise the ocean stratification in more than 90% of the ocean grids at 1° spatial resolution, while salinity changes result in an N^2 increase in only ~58.4% of ocean areas and with more complex spatial variability than for temperature changes (Fig. 4 and Extended Data Fig. 1). On a global average, temperature changes dominate the observed stratification increase (~96.9%; Supplementary Table 3 and Extended Data Fig. 9) but salinity changes play an important role locally (Fig. 4).

In the Pacific Ocean, the low latitudes become more stable than higher latitudes (Fig. 4b) in association with greater surface warming (Extended Data Fig. 1). A stronger stratification increase is found in the eastern rather than western equatorial regions, probably linked to the weakened easterlies and associated reduced upwelling in the eastern Pacific due to the long-term weakening of Walker circulation[35]. Overall, the temperature contribution dominates the stratification increase (~83.1%; Supplementary Table 3). Salinity changes offset effects in the subtropical gyre regions and reinforce the temperature effects within the Intertropical Convergence Zone (ITCZ) and North Pacific (north of 40° N). This behaviour matches the enhancement of existing patterns of broad-scale salinity associated with an intensified global water cycle[8,18].

In the Indian Ocean, the stratification increases are also mainly driven by temperature changes (over 100%), especially along the intersection of the ACC and subtropical cells within 30–50° S, associated with the transport of warm water from the south and then subduction into the deep layers[36]. The thermal influence is partly offset by the salinity increase in the West Indian Ocean[18]. The freshening in the East Indian Ocean strongly reinforces the stratification due to surface warming (Fig. 4), associated with stronger Indonesian throughflow[37].

In the Atlantic Ocean, overall temperature-induced stratification is ~1.6 times greater than the observed total change because it is offset ~42% by basin-wide salinity increases. The large-scale salinization in the Atlantic Ocean (stronger near the surface) is due to the basin-scale atmospheric freshwater transport from the Atlantic to the Pacific Ocean related to the intensification of water cycle[8,18].
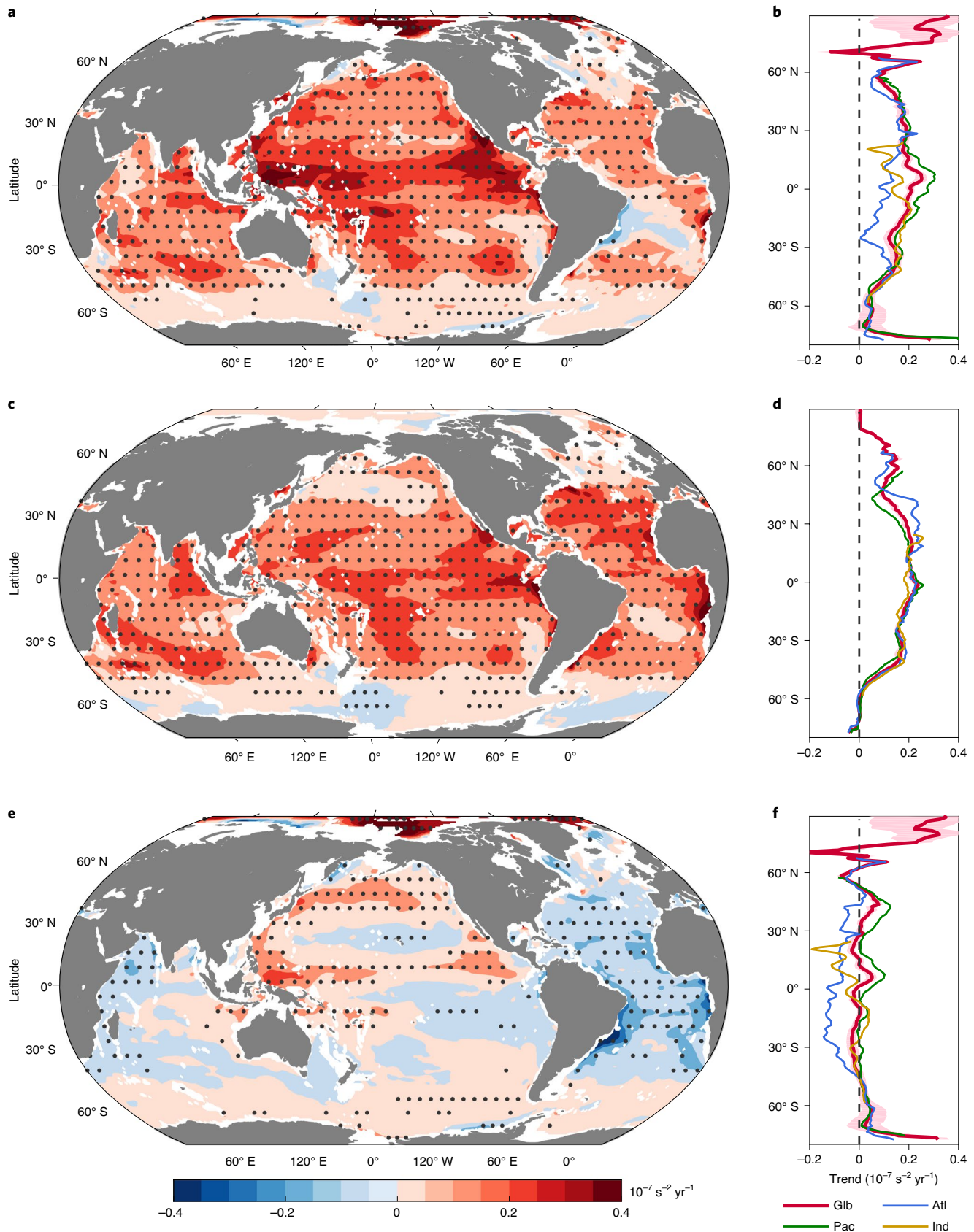
Fig. 4 | Spatial patterns of the 0–2,000 m stratification (N^2) trends and the contributions from temperature and salinity. a–f, Linear trends of 0–2,000 m mean N^2 are calculated for 1960–2018 in **a**, **c** and **e**, where **c** and **e** show the contribution from temperature and salinity, respectively; their zonal averages are shown in **b** (N^2), **d** (temperature contribution) and **f** (salinity contribution). The stippling (**a,c,e**) and shading (**b,d,f**) indicate the regions with statistically significant signals (90% confidence level), with sampling and instrumental errors taken into account.

Changes in the Arctic Ocean are uncertain owing to sparse data although it appears to be becoming more stratified (north of 65° N, 5.4 [2.6, 7.4]%) (Fig. 4a,b,f and Supplementary Table 1). Notable changes in both temperature and salinity are evident north of the Bering Strait and northeast of Greenland (Fig. 4c,e). Stratification is expected to increase in the Arctic Ocean because of polar freshening (Fig. 4f), resulting from increasing net precipitation, freshwater runoff from rivers and (well-observed) glacial ice melting and discharge of ice (that is, Greenland) and the inflow from mid-latitude Pacific waters[38,39].

Warming is the primary determining factor behind the observed stratification increase in the south of 30° S (Fig. 4 and Supplementary Table 3), although observations are not as complete as desirable. For 30−50° S, large ocean warming extends from the surface to 2,000 m (Extended Data Fig. 1b), dominating the observed stratification change[40]. Meanwhile, persistent near-surface freshening is evident since 1960 (Extended Data Fig. 1d). The fresher waters were further subducted into the ocean interior by the mode and intermediate waters[18] and increased the stratification south of 50° S for the upper 200 m to compete with the temperature contribution, resulting in a weak positive stratification trend. Model studies suggest that this salinity-dominant stratification is associated with the northward freshwater transport and can impact the vertical thermal structure in the Southern Ocean[41,42].

Discussion

In this study, we analysed changes in ocean stratification (using N^2) in multiple datasets, finding consistent evidence for overall enhanced stratification in most regions of the world oceans, down to depths of 2,000 m. We also find evidence for considerable spatial complexity. The spatial structure of N^2 implies that previous analyses, which simply computed the density difference between surface and 200-m layers, do not yield an accurate depiction of changing ocean stratification. Our improved observational products allow for more accurate quantification of historical changes in stratification and their uncertainty (such as Extended Data Fig. 10).

Increasing stratification has important climate implications. The expected decrease in ocean ventilation[2,5] could affect ocean heat and carbon uptake[4,10], water mass formation[2] and tropical storm formation and strength[3]. The associated decrease in ocean mixing, moreover, is consistent with a decline in ocean oxygen concentration[5,6], reduced nutrient flux[7] and alteration of marine productivity and biodiversity[7,10,43], as observed. Regions (for example in the North and tropical Pacific and South Atlantic) with the maximum increase in stratification correspond to regions of known de-oxygenation[44]. This is expected, given that more than 80% of observed global ocean oxygen decline is associated with enhanced stratification and consequent weakening of deep-water ventilation and biological depletion associated with the inhibition of nutrient supply[5]. It underscores the consistency between observed physical and geochemical climate change impacts.

Projected future changes in stratification[7,10,45], also have implications for density-driven ocean circulation changes and, in particular, the Atlantic Meridional Overturning Circulation, which already shows some evidence of slowdown[16]. Increased stratification is also expected to increase the westward propagation speed of oceanic Rossby waves in the Pacific, perhaps diminishing decadal Pacific Ocean predictability[46]. Future projections are currently hampered by limitations in current generation climate models in simulating the vertical structure of density changes[9,47], especially because of cryospheric changes, including Greenland and Antarctic ice sheet mass loss[48]. Ocean stratification is nonetheless projected to continue to increase given business-as-usual carbon emissions, as ocean warming and freshwater input by melting glaciers and ice sheets proceeds. Our observational results thus provide important benchmarks for evaluating climate models used for future projections.

Online content

Any methods, additional references, Nature Research reporting summaries, source data, extended data, supplementary information, acknowledgements, peer review information; details of author contributions and competing interests; and statements of data and code availability are available at https://doi.org/10.1038/s41558-020-00918-2.

References

1. Rhein, M. et al. in *Climate Change 2013: The Physical Science Basis* (eds Stocker, T. F. et al.) 215–315 (IPCC, Cambridge Univ. Press, 2013).
2. de Lavergne, C., Palter, J. B., Galbraith, E. D., Bernardello, R. & Marinov, I. Cessation of deep convection in the open Southern Ocean under anthropogenic climate change. *Nat. Clim. Change* **4**, 278–282 (2014).
3. Balaguru, K., Foltz, G. R., Leung, L. R. & Emanuel, K. A. Global warming-induced upper-ocean freshening and the intensification of super typhoons. *Nat. Commun.* **7**, 13670 (2016).
4. DeVries, T., Holzer, M. & Primeau, F. Recent increase in oceanic carbon uptake driven by weaker upper-ocean overturning. *Nature* **542**, 215–218 (2017).
5. Breitburg, D. et al. Declining oxygen in the global ocean and coastal waters. *Science* **359**, eaam7240 (2018).
6. Keeling, R. F., Körtzinger, A. & Gruber, N. Ocean deoxygenation in a warming world. *Annu. Rev. Mar. Sci.* **2**, 199–229 (2010).
7. Fu, W., Randerson, J. T. & Moore, J. K. Climate change impacts on net primary production (NPP) and export production (EP) regulated by increasing stratification and phytoplankton community structure in the CMIP5 models. *Biogeosciences* **13**, 5151–5170 (2016).
8. Durack, P. J. Ocean salinity and the global water cycle. *Oceanography* **28**, 20–31 (2015).
9. Cheng, L., Abraham, J. P., Hausfather, Z. & Trenberth, K. E. How fast are the oceans warming? *Science* **363**, 128–129 (2019).
10. Bindoff, N. et al. in *IPCC Special Report on the Ocean and Cryosphere in a Changing Climate* (eds Pörtner, H.-O. et al.) Ch. 5 (IPCC, 2019).
11. Yamaguchi, R. & Suga, T. Trend and variability in global upper-ocean stratification since the 1960s. *J. Geophys. Res. Oceans* **124**, 8933–8948 (2019).
12. Abraham, J. P. et al. A review of global ocean temperature observations: implications for ocean heat content estimates and climate change. *Rev. Geophys.* **51**, 450–483 (2013).
13. Somavilla, R., González-Pola, C. & Fernández-Diaz, J. The warmer the ocean surface, the shallower the mixed layer. How much of this is true? *J. Geophys. Res. Oceans* **122**, 7698–7716 (2017).
14. Cheng, L. et al. Improved estimates of ocean heat content from 1960 to 2015. *Sci. Adv.* **3**, e1601545 (2017).
15. Cheng, L. et al. Improved estimates of changes in upper ocean salinity and the hydrological cycle. *J. Clim.* https://doi.org/10.1175/JCLI-D-20-0366.1 (2020).
16. Rahmstorf, S. et al. Exceptional twentieth-century slowdown in Atlantic Ocean overturning circulation. *Nat. Clim. Change* **5**, 475–480 (2015).
17. Gleckler, P. J., Durack, P. J., Stouffer, R. J., Johnson, G. C. & Forest, C. E. Industrial-era global ocean heat uptake doubles in recent decades. *Nat. Clim. Change* **6**, 394–398 (2016).
18. Durack, P. J. & Wijffels, S. E. Fifty-year trends in global ocean salinities and their relationship to broad-scale warming. *J. Clim.* **23**, 4342–4362 (2010).
19. Tokarska, K. B., Hegerl, G. C., Schurer, A. P., Ribes, A. & Fasullo, J. T. Quantifying human contributions to past and future ocean warming and thermosteric sea level rise. *Environ. Res. Lett.* **14**, 074020 (2019).
20. Good, S. A., Martin, M. & Rayner, N. A. EN4: quality controlled ocean temperature and salinity profiles and monthly objective analyses with uncertainty estimates. *J. Geophys. Res.* **118**, 6704–6716 (2013).
21. Levitus, S. et al. World ocean heat content and thermosteric sea level change (0–2000 m), 1955–2010. *Geophys. Res. Lett.* https://doi.org/10.1029/2012GL051106 (2012).
22. Balmaseda, M. A., Mogensen, K. & Weaver, A. T. Evaluation of the ECMWF ocean reanalysis system ORAS4. *Q. J. R. Meteorol. Soc.* **139**, 1132–1161 (2013).
23. Ishii, M. & Kimoto, M. Reevaluation of historical ocean heat content variations with time-varying XBT and MBT depth bias corrections. *J. Oceanogr.* **65**, 287–299 (2009).
24. Durack, P. J., Gleckler, P. J., Landerer, F. W. & Taylor, K. E. Quantifying underestimates of long-term upper-ocean warming. *Nat. Clim. Change* **4**, 999–1005 (2014).
25. Trenberth, K. E. The definition of El Niño. *Bull. Am. Meteorol. Soc.* **78**, 2771–2778 (1997).

26. Zheng, F., Zhang, R. & Zhu, J. Effects of interannual salinity variability on the barrier layer in the western-central equatorial Pacific: a diagnostic analysis from Argo. *Adv. Atmos. Sci.* **31**, 532–542 (2014).

27. Qu, T., Song, Y. T. & Maes, C. Sea surface salinity and barrier layer variability in the equatorial Pacific as seen from Aquarius and Argo. *J. Geophys. Res. Oceans* **119**, 15–29 (2014).

28. AchutaRao, K. M. et al. Simulated and observed variability in ocean temperature and heat content. *Proc. Natl Acad. Sci. USA* **104**, 10768–10773 (2007).

29. Chen, X. & Tung, K. K. Global surface warming enhanced by weak Atlantic overturning circulation. *Nature* **559**, 387–391 (2018).

30. Santer, B. D. et al. Causes of differences in model and satellite tropospheric warming rates. *Nat. Geosci.* **10**, 478–485 (2017).

31. Li, X., Xie, S. P., Gille, S. T. & Yoo, C. Atlantic-induced pan-tropical climate change over the past three decades. *Nat. Clim. Change* **6**, 275–279 (2016).

32. Meehl, G. A., Hu, A., Santer, B. D. & Xie, S. P. Contribution of the Interdecadal Pacific Oscillation to twentieth-century global surface temperature trends. *Nat. Clim. Change* **6**, 1005–1008 (2016).

33. Trenberth, K. E. Has there been a hiatus? *Science* **349**, 691–692 (2015).

34. Kosaka, Y. & Xie, S. P. Recent global-warming hiatus tied to equatorial Pacific surface cooling. *Nature* **501**, 403–407 (2013).

35. Tokinaga, H. et al. Regional patterns of tropical Indo-Pacific climate change: evidence of the Walker Circulation weakening. *J. Clim.* **25**, 1689–1710 (2011).

36. Shi, J. R., Xie, S. P. & Talley, L. D. Evolving relative importance of the Southern Ocean and North Atlantic in anthropogenic ocean heat uptake. *J. Clim.* **31**, 7459–7479 (2018).

37. Du, Y. et al. Decadal trends of the upper ocean salinity in the tropical Indo-Pacific since mid-1990s. *Sci. Rep.* **5**, 16050 (2015).

38. Haine, T. W. N. et al. Arctic freshwater export: status, mechanisms, and prospects. *Glob. Planet. Change* **125**, 13–35 (2015).

39. Carmack, E. C. et al. Freshwater and its role in the arctic marine system: sources, disposition, storage, export, and physical and biogeochemical consequences in the Arctic and global oceans. *J. Geophys. Res. Biogeosci.* **121**, 675–717 (2016).

40. Swart, N. C., Gille, S. T., Fyfe, J. C. & Gillett, N. P. Recent Southern Ocean warming and freshening driven by greenhouse gas emissions and ozone depletion. *Nat. Geosci.* **11**, 836–841 (2018).

41. Purkey, S. G. & Johnson, G. C. Antarctic bottom water warming and freshening: contributions to sea level rise, ocean freshwater budgets, and global heat gain. *J. Clim.* **26**, 6105–6122 (2013).

42. Haumann, F. A., Gruber, N., Münnich, M., Frenger, I. & Kern, S. Sea-ice transport driving Southern Ocean salinity and its recent trends. *Nature* **537**, 89–92 (2016).

43. Boyce, D. G., Lewis, M. R. & Worm, B. Global phytoplankton decline over the past century. *Nature* **466**, 591–596 (2010).

44. Schmidtko, S., Stramma, L. & Visbeck, M. Decline in global oceanic oxygen content during the past five decades. *Nature* **542**, 335–339 (2017).

45. Capotondi, A., Alexander, M. A., Bond, N. A., Curchitser, E. N. & Scott, J. D. Enhanced upper ocean stratification with climate change in the CMIP3 models. *J. Geophys. Res. Oceans* **117**, C04031 (2012).

46. Li, S. et al. The Pacific Decadal Oscillation less predictable under greenhouse warming. *Nat. Clim. Change* **10**, 30–34 (2019).

47. Kuhlbrodt, T. & Gregory, J. M. Ocean heat uptake and its consequences for the magnitude of sea level rise and climate change. *Geophys. Res. Lett.* https://doi.org/10.1029/2012GL052952 (2012).

48. Collins, M. et al. in *Climate Change 2013: The Physical Science Basis* (eds. Stocker, T. F. et al.) 1029–1136 (IPCC, Cambridge Univ. Press, 2013).

Methods

Data sources and processing. The primary dataset used in this study is an ocean objective analysis from the IAP for 1960 to present. These data are available with $1° \times 1°$ horizontal resolution and 41 vertical levels for the upper 0–2,000 m. The key advantages of these analyses are the application of the community-recommended instrumental bias correction (XBT correction), the advanced gap-filling algorithm that is unbiased in reconstructing decadal/multidecadal scale temperature/salinity change since 1960 for the upper 2,000 m and the careful evaluation using recent Argo data[14,15].

Four other independent datasets of temperature and salinity are also used: three objectively analysed products of in situ observations, from (1) the EN4 (ref. [20]) from 1960 to 2018; (2) Ishii data[23,49] for 1960–2018; (3) the pentad NCEI product from 1955 to 2018[21]; and (4) an ocean reanalysis product, which assimilates various observations into an ocean model, Ocean Reanalysis System 4 (ORAS4)[22] for 1960–2017. The in situ fields are converted into the variables of conservative temperature and absolute salinity, to compute the potential density and squared buoyancy frequency based on TEOS-10 standard[50].

Three observational SST gridded datasets used span from 1960 to 2018: (1) ERSSTv.5 (ref. [51]) $(2° \times 2°)$; (2) COBE2 (ref. [52]) $(1° \times 1°)$; and (3) HadSST3 data[53,54] $(5° \times 5°)$. A climatology with seasonal cycle was constructed for 1981 to 2010 and the anomalies computed by removing the climatology.

Stratification calculation. The stratification is computed as the squared buoyancy frequency:

$$N^2 = gE = g\left[-\left(\frac{1}{\rho}\right)\left(\frac{\partial \sigma_n}{\partial z}\right) \right]$$

where ρ, σ_n and g denotes seawater density, local potential density anomaly and gravity acceleration, respectively. N, the Brunt–Väisälä frequency, represents the intrinsic frequency of internal waves. The more stratified the water column, the higher the static stability and the higher the buoyancy frequency. In this study, N^2 is computed according to the equation of state (TEOS-10) (ref. [50]):

$$N^2(\Theta, S_A) = g\left(\alpha^\ominus \Theta_z - \beta^\ominus S_{A_z} \right)$$

where $\alpha^\ominus$ and $\beta^\ominus$ denote the thermal expansion and saline contraction coefficients, respectively. The subscript (z) represents the vertical gradients.

To reduce the noise in the vertical gradient computation: (1) the vertical levels are interpolated into higher vertical resolution (5-m interval) based on a weighted-parabola method by Reiniger and Ross[55], which has a smoothing effect and is widely used in the ocean community; (2) the three-point binomial weighted (0.25–0.5–0.25) smoothing is then applied.

The percentage change of N^2 is calculated based on a climatological mean state during 1981–2010. However, using alternative climatological averaging periods yields negligible (<5%) differences—see Supplementary Table 4.

Separating T and S contributions to stratification. To evaluate the relative contributions of the temperature (Θ) and salinity (S_A) to the change in N^2, we compute their contribution separately as follows:

$$T : N^2_\Theta = N^2\left(\bar{\Theta} + \Theta', \overline{S_A} \right)$$

$$S : N^2_{S_A} = N^2\left(\bar{\Theta}, \overline{S_A} + S_A' \right)$$

where, N^2_Θ and $N^2_{S_A}$ represents the N^2 change related to thermal and saline effects, respectively. Here, overbars and primes denote climatological mean and deviations from the mean. Owing to the nonlinearity of this equation, the contributions of T and S cannot be fully separated. Here, we removed the climatologies to obtain the empirical contribution from temperature and salinity anomalies, named the anomalous $N^{2'}_\Theta$ and $N^{2'}_{S_A}$, respectively. Thus, N^2 can be approximated:

$$N^2(\Theta, S_A)' = N^{2'}_\Theta + N^{2'}_{S_A} + \text{Res} = N^2(\Theta', \bar{S}_A)' + N^2(\bar{\Theta}, S_A')' + \text{Res}$$

where Res denotes the residual arising from the interaction between temperature and salinity changes. To verify the accuracy of this separation, Extended Data Fig. 9a (versus Fig. 4) shows the difference between linear trends of N^2 and the sum the first two terms on the right side of this equation and reveals a negligible impact of Res on spatial trend. The contribution of Res on basin means is again quantified in Extended Data Fig. 9b, suggesting a negligible impact. Both confirm the validity of this separation.

Uncertainty estimate for N^2. N^2 depends on observed temperature and salinity fields, and data coverage (both horizontal and vertical sampling) and the instrument quality of the observations are the two primary sources of error. The IAP mapping method is an Ensemble Optimal Interpolation approach with an objective error analysis procedure[56]. It results in 30 ensemble members for temperature and 40 ensemble members for salinity, from which the uncertainty

associated with horizontal sampling and instrumental error can be quantified. A caveat, to be addressed in future, is the impact of systematic biases.

Uncertainty error stems from relatively low vertical resolution of past ocean profile observations and its changes over time (Extended Data Fig. 4). Uncertainties from the vertical interpolation used to standardize the profiles is tested by subsampling 12 high-resolution static temperature and salinity climatologies according to observational masks from 1960 to 2017 (ref. [57]) (detailed in the Supplementary Information). The high-resolution climatologies are constructed by collecting all high-resolution profiles since 1960 (mean resolution <5 m at upper 200 m, <10 m within 200–1,000 m and <25 m within 1,000–2,000 m). The resampled fields are input into the IAP mapping technique and then the resultant reconstructions with and without vertical resampling are contrasted to quantify the vertical sampling errors associated with Reiniger and Ross, linear interpolation and spline methods for the 12 ensemble members for both temperature and salinity fields.

To combine the horizontal sampling and instrumental uncertainty with vertical sampling uncertainty, a Monte Carlo approach is used to generate the final uncertainty range in N^2 (illustrated in Supplementary Fig. 3). A total of 5,000 realizations of N^2 are generated on the basis of the available ensemble, where each realization is calculated on the basis of a randomly selected ensemble member from each error source. Their ensemble median is used along with the [5%, 95%] range of N^2 based on 5,000 realizations and hence the skew of the error distribution can be accounted for (Table 1 and Extended Data Fig. 10).

Uncertainty of linear trends. The linear trends were computed by using the ordinary least squares, with error bars accounting for the reduction of degrees of freedom assuming the residuals follow first-order autoregressive model AR(1). For the uncertainty level of the trends, the 90% confidence interval (CI) is presented throughout this study.

Data availability

The data are available in the following links. IAP (http://159.226.119.60/cheng/); NCEI (https://www.nodc.noaa.gov/OC5/3M_HEAT_CONTENT/); EN4 (https://www.metoffice.gov.uk/hadobs/en4/download-en4-2-1.html); Ishii (https://climate.mri-jma.go.jp/pub/ocean/ts/); and ORAS4 (http://apdrc.soest.hawaii.edu/datadoc/ecmwf_oras4.php). For SST: ERSSTv.5 (https://www1.ncdc.noaa.gov/pub/data/cmb/ersst/v5/netcdf/); COBE2 (https://psl.noaa.gov/data/gridded/data.cobe2.html); and HadSST3 (https://www.metoffice.gov.uk/hadobs/hadsst3/data/download.html). Also, data are available from the corresponding author on reasonable request. Raw figures and data are available from http://159.226.119.60/cheng/ and https://doi.org/10.6084/m9.figshare.12771116. Source data are provided with this paper.

Code availability

The source codes used to make the calculations and plots in this paper are available at http://159.226.119.60/cheng/ and from the corresponding author on request.

References

49. Ishii, M. et al. Accuracy of global upper ocean heat content estimation expected from present observational data sets. *SOLA* **13**, 163–167 (2017).
50. IOC, SCOR & IAPSO *The International Thermodynamic Equation of Seawater—2010: Calculation and Use of Thermodynamic Properties* (UNESCO, 2010).
51. Huang, B. et al. Extended reconstructed sea surface temperature, version 5 (ERSSTv5): upgrades, validations, and intercomparisons. *J. Clim.* **30**, 8179–8205 (2017).
52. Hirahara, S., Ishii, M. & Fukuda, Y. Centennial-scale sea surface temperature analysis and its uncertainty. *J. Clim.* **27**, 57–75 (2014).
53. Kennedy, J. J., Rayner, N. A., Smith, R. O., Parker, D. E. & Saunby, M. Reassessing biases and other uncertainties in sea surface temperature observations measured in situ since 1850: 1. Measurement and sampling uncertainties. *J. Geophys. Res. Atmos.* https://doi.org/10.1029/2010JD015218 (2011).
54. Kennedy, J. J., Rayner, N. A., Smith, R. O., Parker, D. E. & Saunby, M. Reassessing biases and other uncertainties in sea surface temperature observations measured in situ since 1850: 2. Biases and homogenization. *J. Geophys. Res. Atmos.* https://doi.org/10.1029/2010JD015220 (2011).
55. Reiniger, R. F. & Ross, C. K. A method of interpolation with application to oceanographic data. *Deep Sea Res.* **15**, 185–193 (1968).
56. Cheng, L. & Zhu, J. Benefits of CMIP5 multimodel ensemble in reconstructing historical ocean subsurface temperature variations. *J. Clim.* **29**, 5393–5416 (2016).
57. Cheng, L. & Zhu, J. Uncertainties of the ocean heat content estimation induced by insufficient vertical resolution of historical ocean subsurface observations. *J. Atmos. Ocean. Technol.* **31**, 1383–1396 (2014).

Author contributions

L.C. initiated and conceptualized this study and performed the subsample test. G.L. performed all the stratification analyses. All authors contributed to the figure generation, interpretation of results and the preparation of the manuscript.

Competing interests

The authors declare no competing interests.

## Additional information

Extended data is available for this paper at https://doi.org/10.1038/s41558-020-00918-2.

Supplementary information is available for this paper at https://doi.org/10.1038/s41558-020-00918-2.

Correspondence and requests for materials should be addressed to L.C. or J.Z.

Reprints and permissions information is available at www.nature.com/reprints.
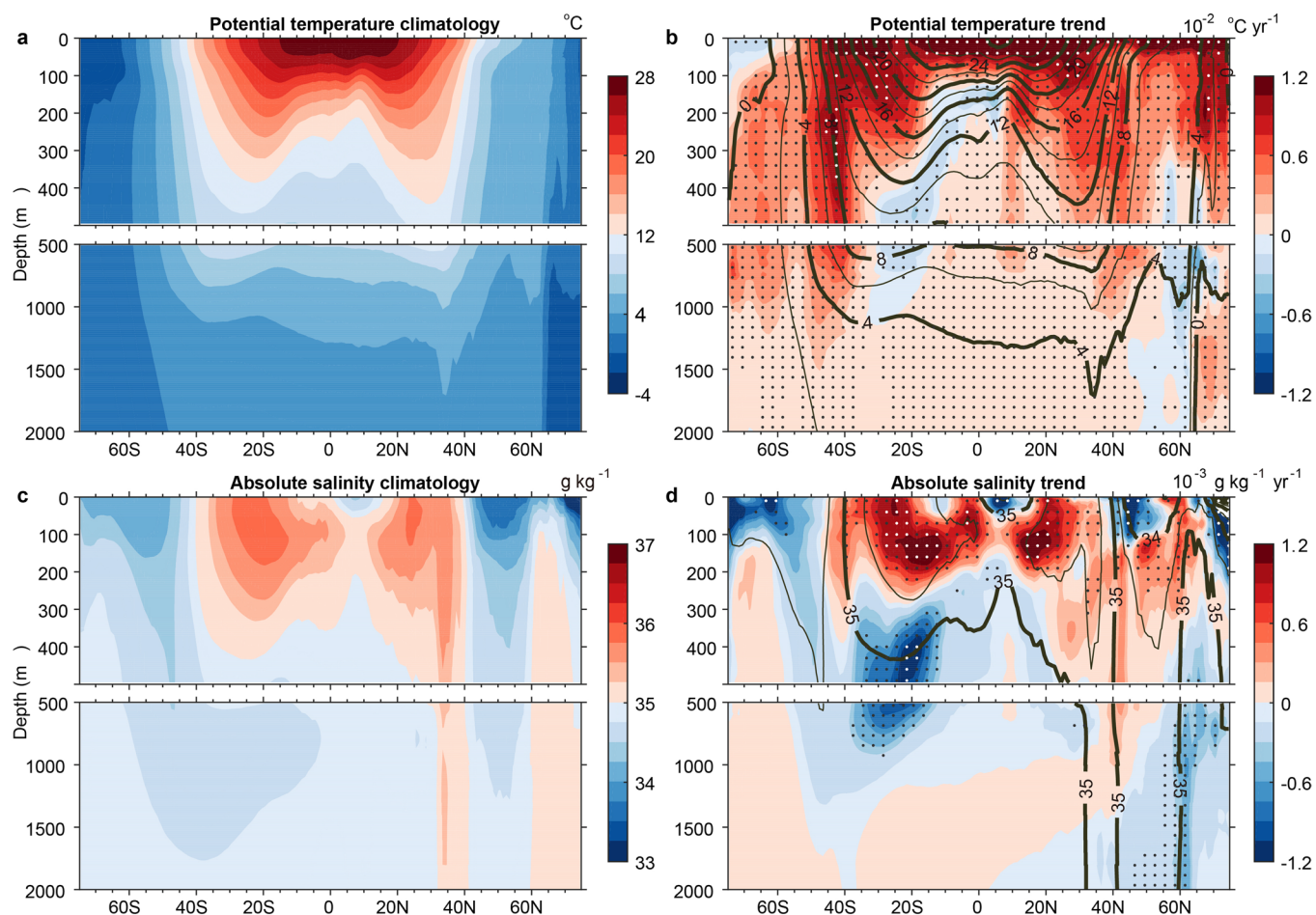
Extended Data Fig. 1 | Climatological means and long-term linear trends of ocean temperature and salinity. a, Climatological mean and **b**, linear trend of zonal mean potential temperature. **c**, Climatological mean and **d**, linear trend of zonal mean absolute salinity. The stippled areas in **b** and **d** denote the signals significant at 90% confidence level.
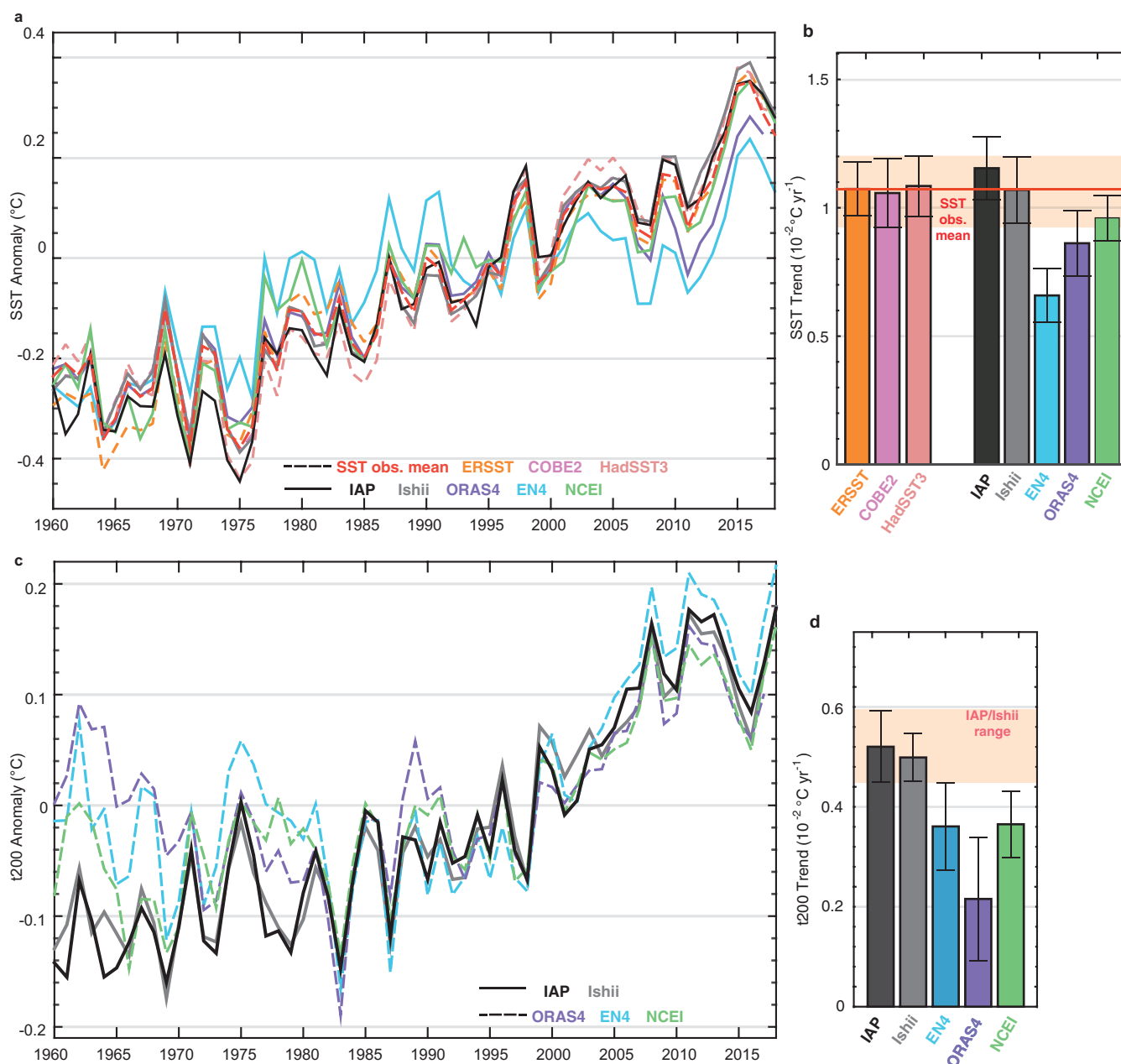
Extended Data Fig. 2 | Temperature anomaly time series and linear trends at surface and 200 m from 1960 to 2018 based on multiple datasets. a, Time series and **b**, linear trends of sea surface temperature change. **c**, Time series and **d**, linear trends of 200 m temperature change. All time series are relative to a 1981–2010 baseline. Error bar in **b** and **d** denotes the 90% confidence interval of linear trend.
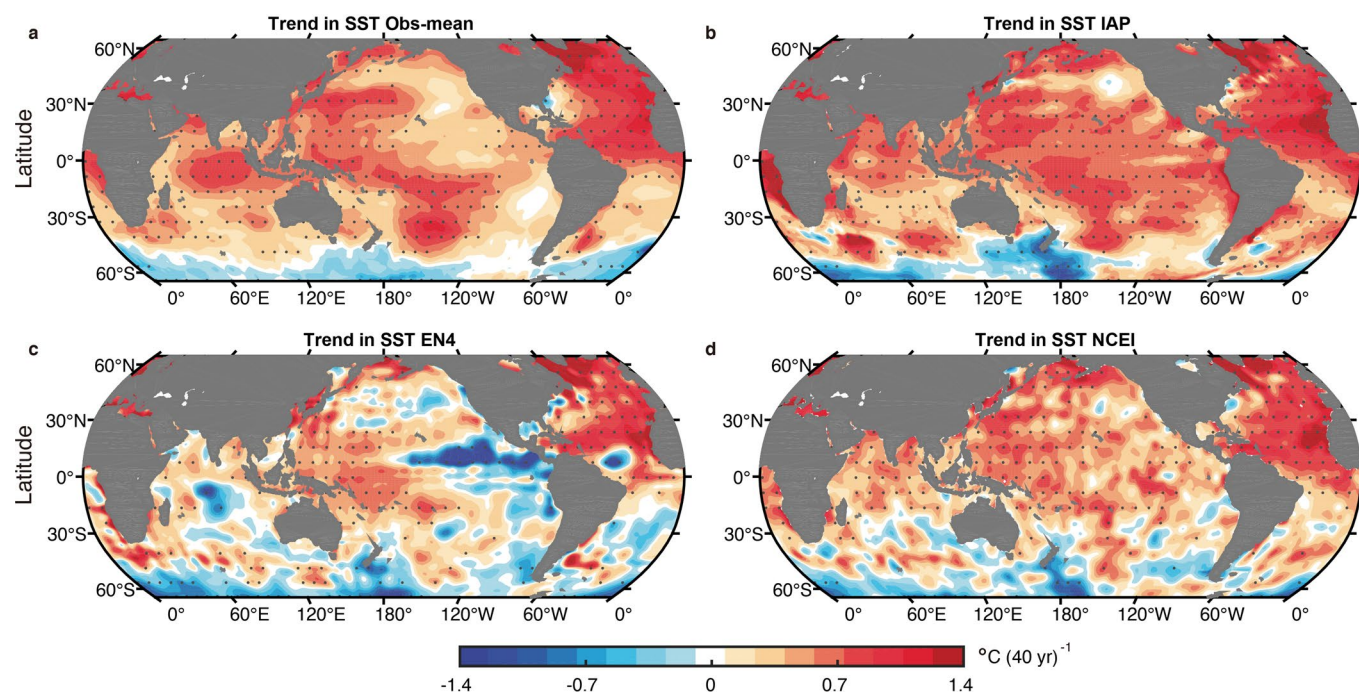
Extended Data Fig. 3 | Spatial patterns of linear trend in the annual SST for different datasets from the 1971 to 2010. a is the observational mean based on three independent SST products, including ERSST, COBE2, and HadSST3, **b** is IAP, **c** is EN4, and **d** is NCEI data. The stippled areas in **a–d** denote the signals significant at 90% confidence level.
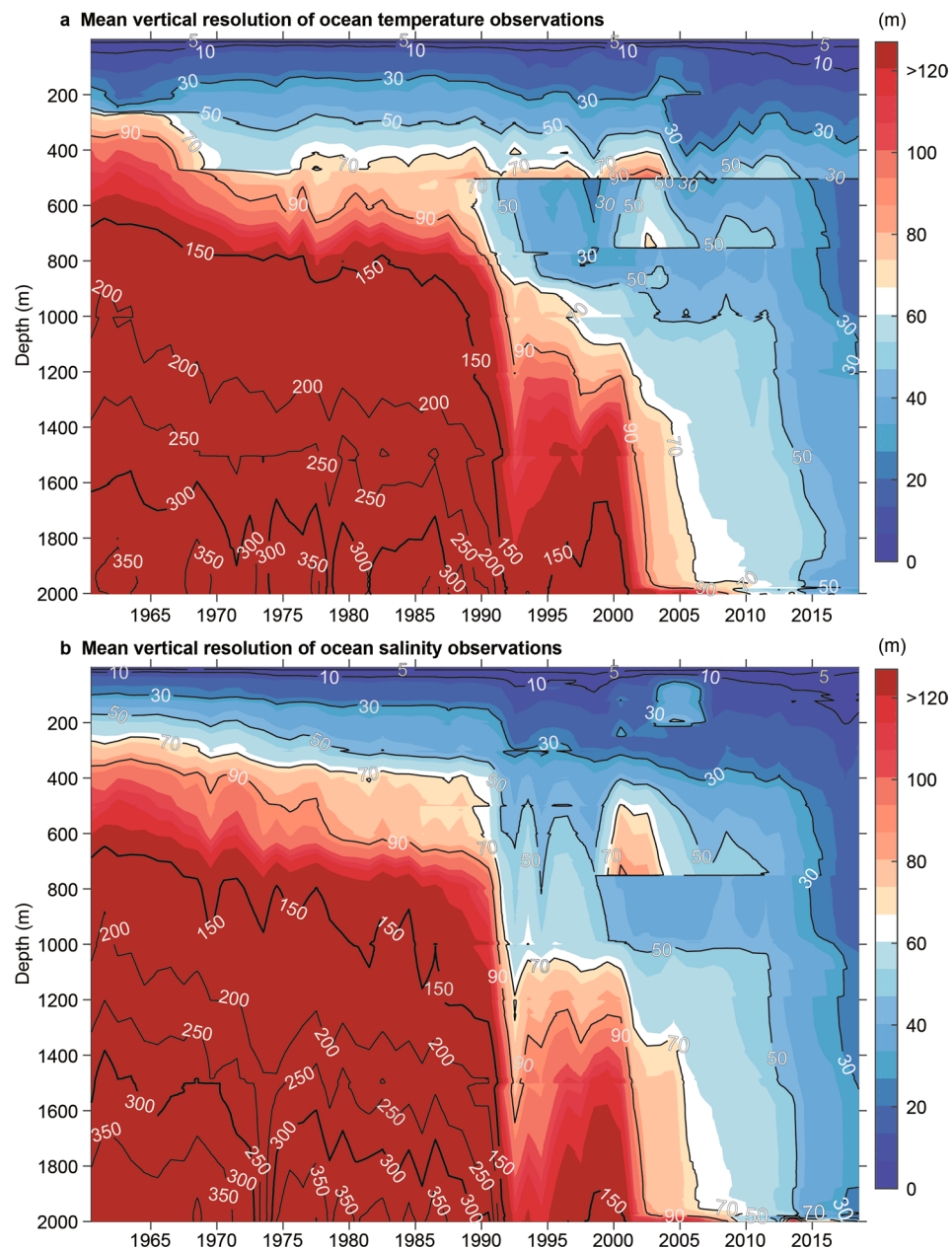
Extended Data Fig. 4 | Annual mean vertical resolution at depths for all *in situ* temperature and salinity observations within 0–2000 m from 1960 to 2018. Annual mean vertical resolution at depths for all in situ temperature **a** and salinity **b** observations within 0–2000 m from 1960 to 2018.
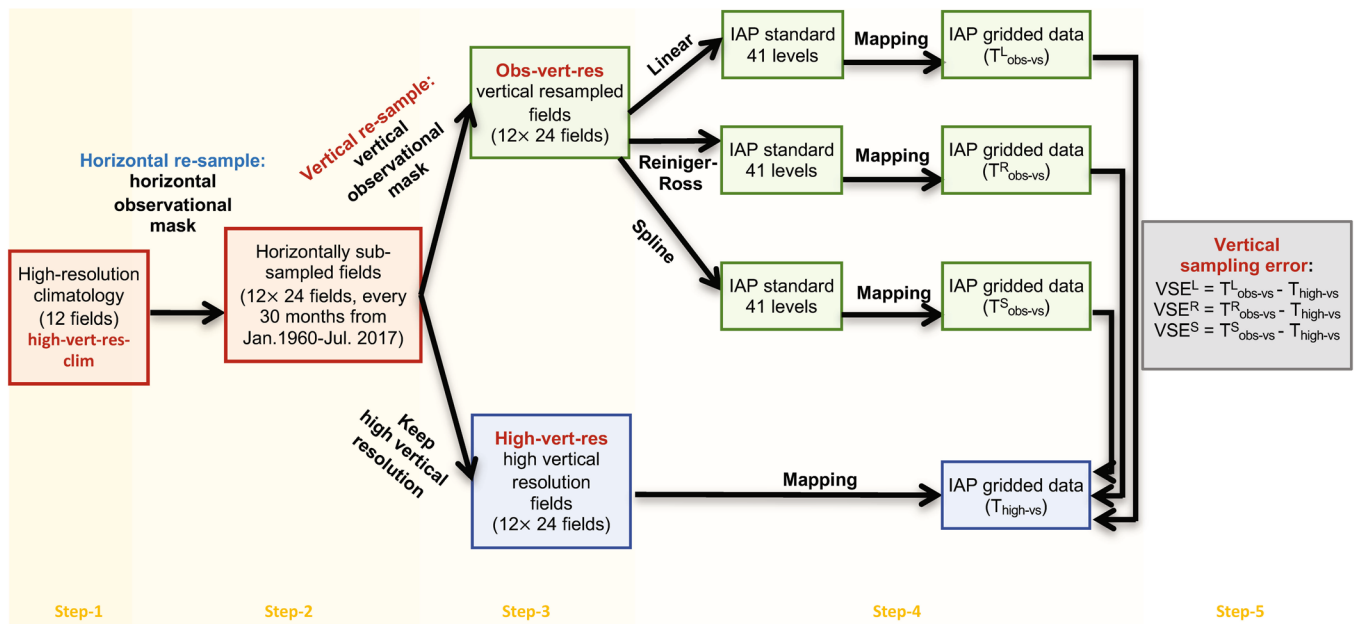
Extended Data Fig. 5 | A schematic of the "vertical subsample test". This test is used to quantify the impacts of vertical resolution in ocean profile observation and vertical interpolation methods on the gridded product (IAP gap-filling method). Temperature and salinity data are processed with the same method.
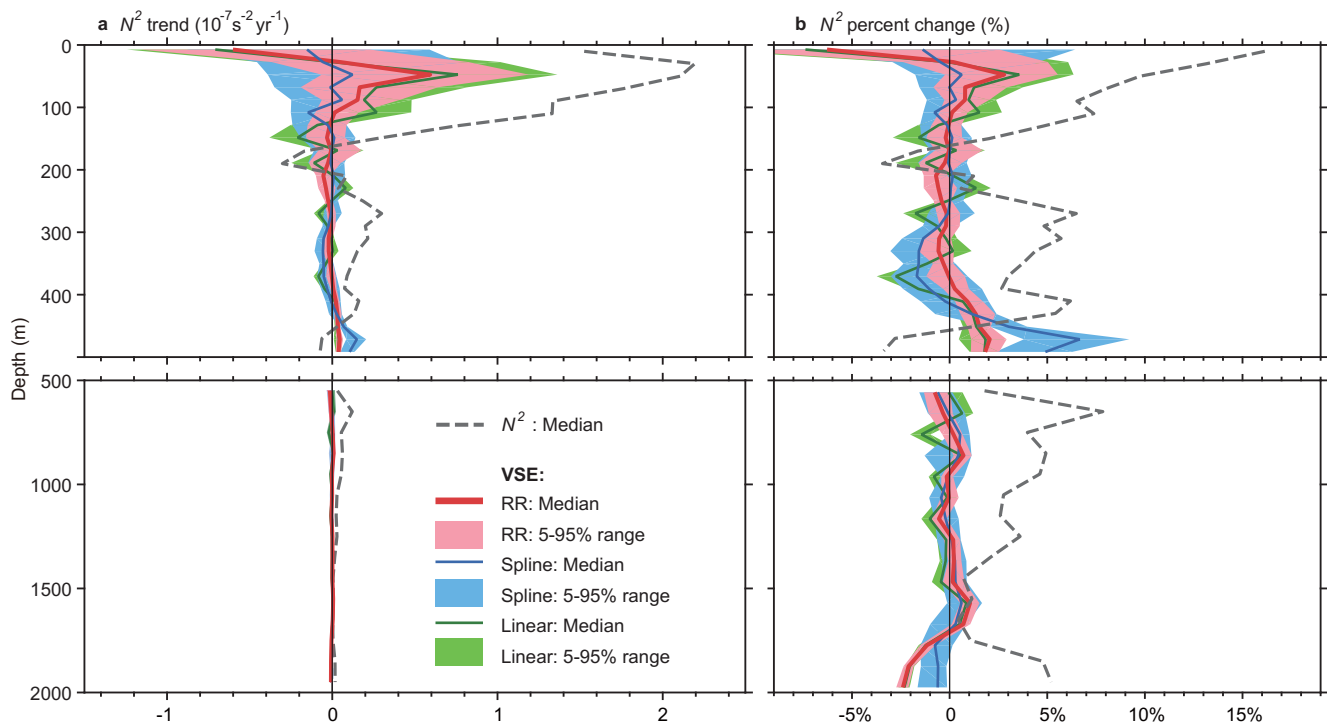
Extended Data Fig. 6 | Trends and per cent changes in global mean N^2 vertical sampling errors from 1960 to 2018 for three interpolation methods.
**a**, Linear trends of N^2 bias at each depth from surface to 2000 m with an interval of 20 m at upper 500 m (100 m below 500 m) (same as Fig. 2a); **b** is same as **a** but for percentages of long-term changes relative to the 1981–2010 average of global mean N^2. Three interpolation methods are included: Reiniger-Ross, Spline, and Linear interpolation. The dotted lines denote the observed N^2 estimates. The shadings are 90% confidence intervals from 5000 realizations.
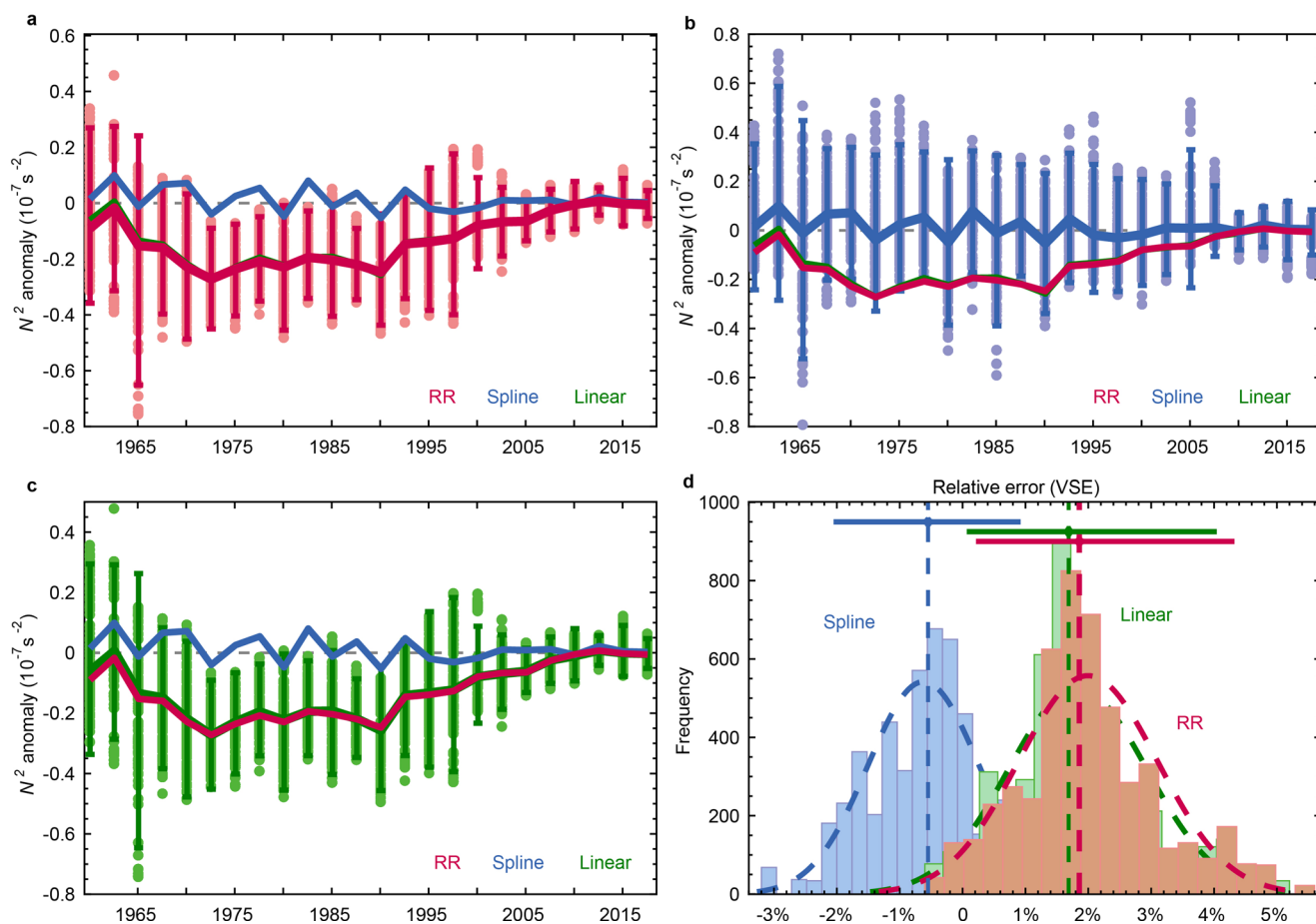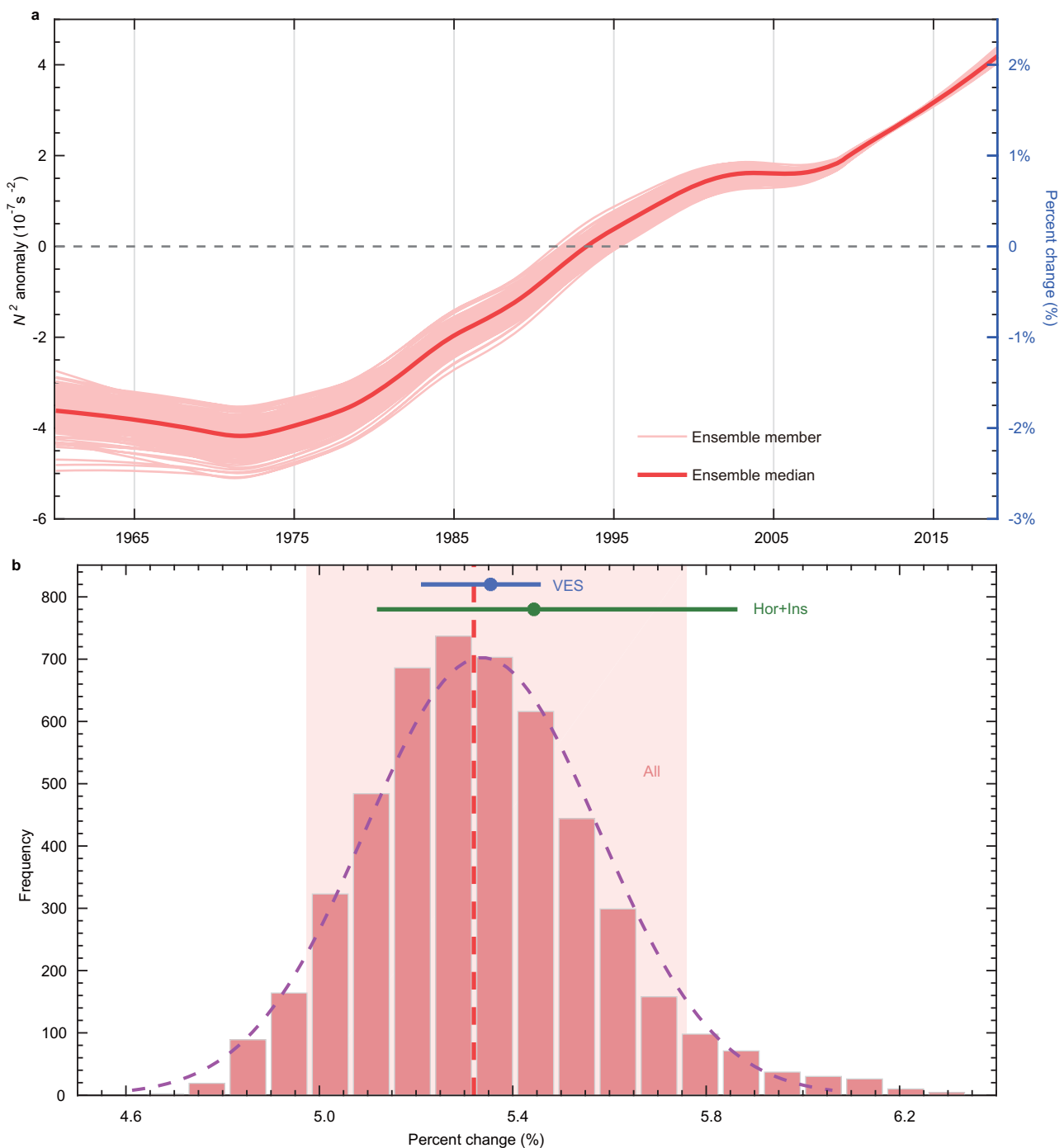
Extended Data Fig. 7 | Global 0–2000 m mean N^2 vertical sampling errors (VSE) associated with different vertical interpolation methods. a for Reiniger-Ross (RR) method, **b** for spline interpolation and **c** for linear interpolation. **d**, Relative error in N^2 changes with three different interpolation methods based on 5000 realizations. The VSE for different T/S high-resolution climatology fields subsampled by historical observation locations are shown as dots, with the solid line and the error bar for the median and 90% confidence interval (CI), respectively. The sticks in (**d**) denote the [5%, 95%] CI of the linear trends based on all realizations using Monte Carlo approach. The fitted Gaussian distribution is included for comparison in (**d**).
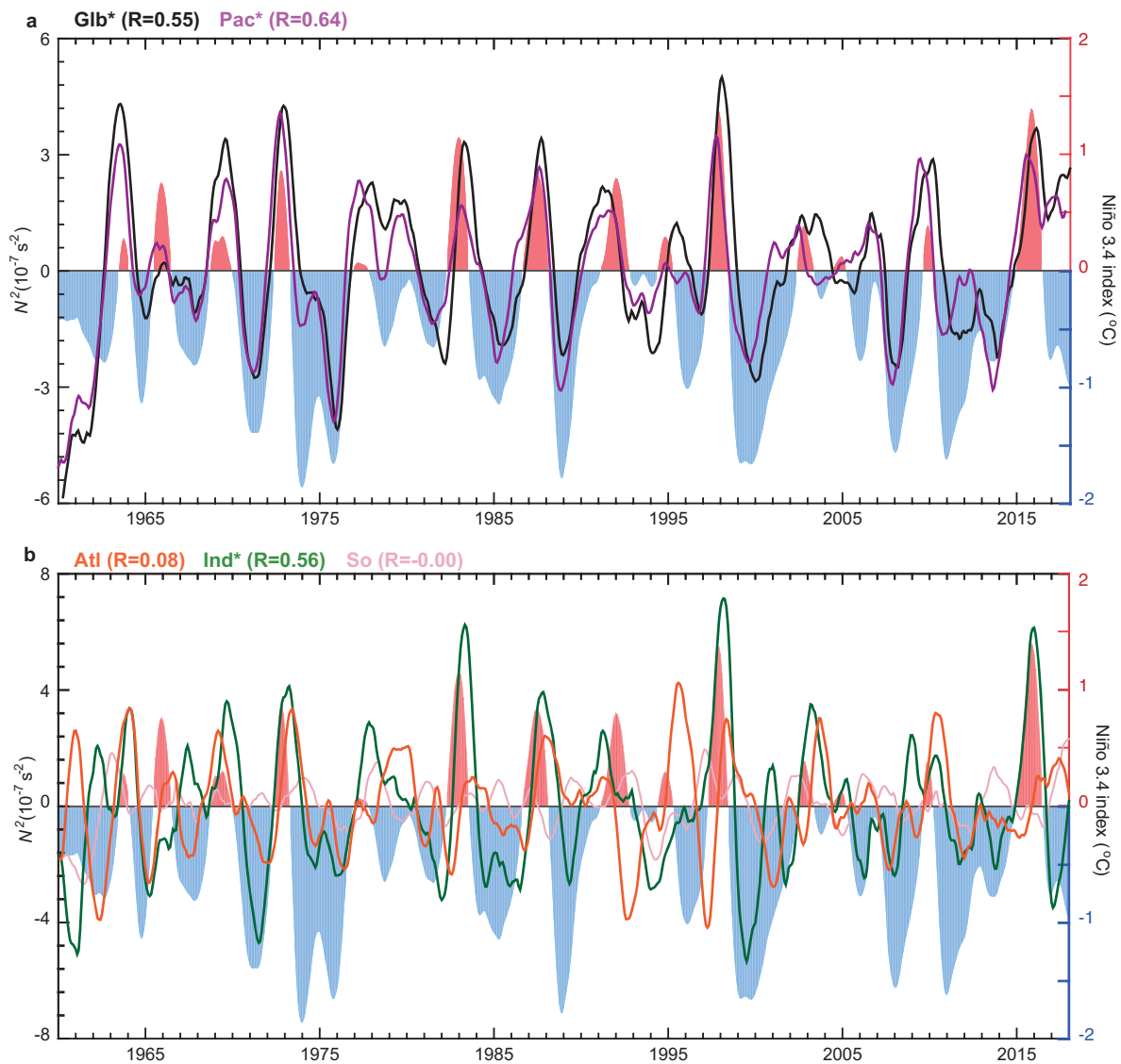
Extended Data Fig. 8 | Annual mean 0–2000 N^2 anomaly compared with the Niño 3.4 index. a for the Global (Glb) and Pacific (Pac) Ocean, **b** for Atlantic (Atl), Indian (Ind) and Southern (So) oceans. For N^2 time series, a high-pass filter with cut-off frequency of 1/102 (period of 8.5 years) is applied. To gain better illustration of interannual variability, all the time series are smoothed by a 13-month running smoother[17] weighted by (1, 6, 19, 42, 71, 96, 106, 96, 71, 42, 19, 6, 1)/576. The correlation between Niño 3.4 index (shading) and N^2 time series (solid lines) are provided at zero lag and * sign means it is statistically significant at the 90% confidence level. Niño3.4 index is obtained from the National Oceanic and Atmospheric Administration Climate Prediction Center (NOAA/CPC) (https://psl.noaa.gov/data/correlation/nina34.data).
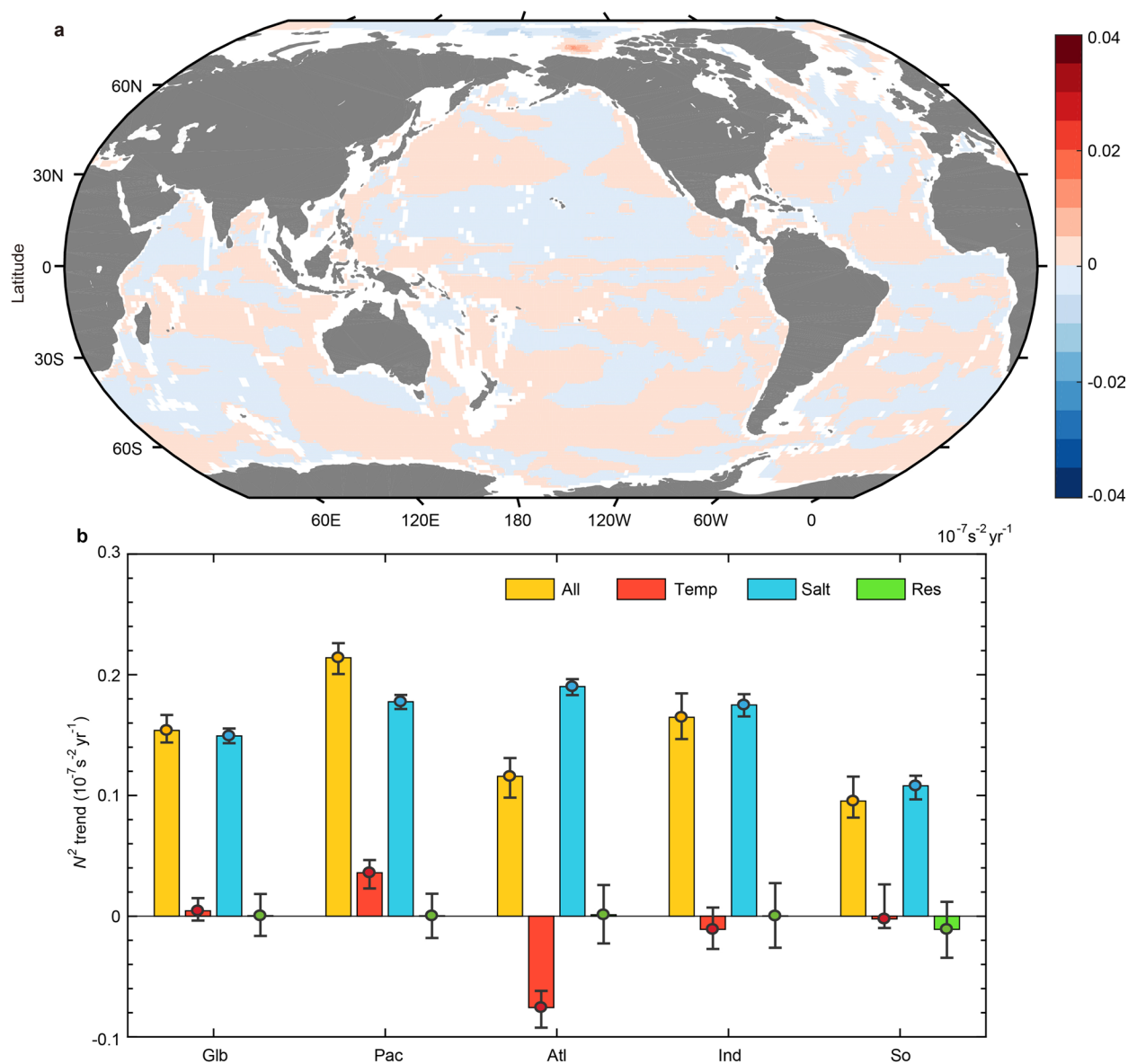
Extended Data Fig. 9 | Results of decomposing analysis of 0–2000 m mean N^2 change. a, Spatial pattern of residual term (*Res*). **b**, Basin-mean linear trends of the observed change and its contributors (caused by the temperature, salinity and *Res* changes). The *Res* is calculated by the difference between the observed linear trends in N^2 (see in Fig. 4a) and the sum of temperature and salinity contributions (see Fig. 4b, c). The dot and the error bar in panel (**b**) denote the median and 90% confidence interval, respectively.

Extended Data Fig. 10 | Ensemble members of 0–2000 m mean N^2 time series and frequency distribution of their trends. a, 5000 realizations of global mean N^2 time series and its ensemble median. **b**, Distribution of the estimated per cent changes of N^2 from these 5000 realizations, with their ensemble median and 90% confidence interval (CI) shown in dashed red line and pink shading, respectively. The per cent changes are relative to 1981–2010 climatological N^2. The fitted Gaussian distribution is included for comparison. The blue bar indicates the estimate (median and 90% CI) when only VES are taken into account in creating 5000 realizations; the green bar indicates the results when only horizonal and instrumental errors are taken into account.